EurJIC
European Journal of Inorganic Chemistry

Research Article
doi.org/10.1002/ejic.202500170

Chemistry Europe
European Chemical Societies Publishing

www.eurjic.org

Synthesis, Characterization, and Electrochemical Properties of Tri- and Tetranuclear Co^{III}-Oxo Complexes

Timo Fockenberg, Niklas Sülzner, Hatem M. A. Amin, Christoph Wölper, Christof Hättig, and Stephan Schulz*

Heterocubane-type complexes containing a central $[Co^{III}_4O_4]$ core have received increasing interest as surface cutouts of active spinel-type Co_3O_4 water splitting catalysts. The synthesis of a series of tetranuclear ($[Co_4O_4(O_2CR)_4(py)_4]$ (R = Me **1**, Et **2**, *n*-Pr **3**)) and trinuclear Co(III) carboxylate complexes $[Co^{III}_3(\mu_3\text{–}O)(\mu_2\text{–}OH)(O_2CR)_3(py)_5](NO_3)_2$ (R = *i*-Pr **4**, *t*-Bu **5**) and their structural (single-crystal X-ray diffraction) and spectroscopic (except **5**, ^{1}H NMR, UV/vis, IR) characterization is reported. Quantum chemical calculations using density functional theory show that the relative stability of the tetranuclear complexes versus the trinuclear complexes decreases with increasing steric demand of the carboxylate ligand. In addition, the UV/vis and IR spectra of the tetranuclear complexes are calculated to deconvolute contributions from the carboxylate ligands and the Co-oxo core. Furthermore, the electrochemical properties of the complexes **1**–**4** are studied by cyclic voltammetry, demonstrating that the redox potential of the complexes correlates with the steric demand of the carboxylate ligand.

1. Introduction

Catalytic oxidation reactions play a pivotal role in the chemical industry, where selectivity, yield, and efficiency are crucial for the viability of industrial chemical processes,[1] as well as in academic research.[2,3] Extensive studies were performed in order to understand the catalytic mechanism in detail, and based on this knowledge, to enable the rational design of efficient use of naturally abundant catalysts. Cobalt oxides are recognized as one of the most efficient, nonprecious catalysts for industrially relevant oxidation catalysis. For example, spinel-type Co_3O_4 nanoparticles have been shown to be effective catalysts for heterogeneous oxidation reactions, including water electrolysis and alcohol oxidation.[4–7] In such oxidation reactions, Co–O species with an oxidation state of +III or higher are assumed as the active sites,[8] but detailed mechanistic information is still lacking. To better understand the catalytic reaction mechanism and the nature of active species, molecular cluster compounds have received increasing attention as model systems for their heterogeneous counterparts. Molecular model systems allow a precise control of the chemical composition, and more importantly, the specific metal oxidation states, facilitating different spectroscopic analyses and computational studies, which are necessary to understand structure–activity correlations in more detail.[9–11]

Among others, heterocubane-type $[Co^{III}_4O_4]$ complexes have been intensively studied as persuasive model systems as they are structurally similar to a subunit of extended CoO_x and have a multimetallic nature.[12,13] First studies in 1998 by Beattie et al. on isolated homogeneous cobalt complexes revealed the formation of a variety of high-valent states of Co-oxo intermediates during oxidation reactions.[14] Das et al. established a high-yield method for the synthesis of $[Co^{III}_4O_4]$ heterocubane-type complexes[15] and also conducted extensive research on the thermal oxidation catalysis using different cobalt-oxo complexes. They demonstrated the catalytic activity of trimeric Co(III) complexes immobilized on chemically modified silica (CMS) for the selective aerobic oxidation of alkyl aromatics,[16] while heterocubane-type $[Co^{III}_4O_4]$ complexes were found to catalytically oxidize (with a given oxidant) α-pinene (O_2),[15] ethyl benzene, and p-xylene (O_2),[17–19] as well as benzylic alcohols (*tert*-butyl hydroperoxide(TBHP)).[20] Even higher selectivities and conversion rates were achieved by immobilization of these $[Co^{III}_4O_4]$ complexes on CMS, i.e., for the heterogeneous oxidation of benzyl alcohols and secondary aliphatic alcohols with TBHP,[21] α-pinene with O_2 (air),[22] styrene with TBHP, and diphenyl methane with TBHP, H_2O_2, or NaOCl, respectively.[23]

$[Co^{III}_4O_4]$ heterocubane-type clusters have also been used for the oxygen evolution reaction (OER) in alkaline media. Britt et al. and Nocera et al. demonstrated the reversible formation of tetravalent Co^{IV} in the one-electron oxidation product

T. Fockenberg, H. M. A. Amin, C. Wölper, S. Schulz
Institute of Inorganic Chemistry
University of Duisburg-Essen
Universitätsstr. 5-7, 45141 Essen, Germany
E-mail: stephan.schulz@uni-due.de

N. Sülzner, C. Hättig
Lehrstuhl für Theoretische Chemie
Ruhr-Universität Bochum
Universitätsstraße 150, 44801 Bochum, Germany

S. Schulz
Center for Nanointegration Duisburg-Essen (CENIDE)
University of Duisburg-Essen
Carl-Benz-Straße 199, 47057 Duisburg, Germany

Supporting information for this article is available on the WWW under https://doi.org/10.1002/ejic.202500170

Research Article
doi.org/10.1002/ejic.202500170

Chemistry Europe
European Chemical Societies Publishing

$[Co^{IV}Co^{III}_3O_4(OAc)_4(py)_4]^+$ using X-ray diffraction and electron paramagnetic resonance (EPR) spectroscopy and reported that the properties of this state resemble that of the CoO_x film.[24,25] Nocera et al. and Tilley et al. also found indications for the involvement of higher Co oxidation states under OER conditions, presumably $[Co^{IV}_2Co^{III}_2O_4]$ or $[Co^{V}Co^{III}_3O_4]$.[9,26] Moreover, Tilley and co-workers reported that hydrocarbon C–H oxidation using $[Co_4O_4(OAc)_4(py)_4][BF_4]$ most likely occurs via concerted proton–electron transfer.[27] These examples showcase the suitability of $[Co_4O_4]$ heterocubane-type complexes for oxidation reactions.

Notably, the chemical and electronic properties of the $[Co_4O_4]$ complexes can be altered by modification of the organic substituents. Previous studies primarily focused on the *para*-functionalization of the pyridine ligand by use of alkyl, cyano, dimethylamino, methoxy, ester, halide, and vinyl groups with different steric and electronic properties.[18,20,28–33] Moreover, chelating ligands containing pyridine moieties were introduced, e.g., bi(2-pyridyl) ketone, 2,2′-bipyridine, 2-pyridone, 7-azaindole, 2-pyridinemethanol, 2,6-pyridinedimethanol, which allowed the variation of the pyridine to acetate ratio while the cubic $[Co^{III}_4O_4]$ core is preserved.[10–12,28,34,35] In contrast, the variation of the acetate (OAc) ligand was less studied and primarily focused on modifying the electronic properties of the ligand by introducing electron-withdrawing substituents, e.g., halides or benzoic acid derivatives (trifluoroacetate, 4-nitro/chlorobenzoate, and chloro/bromo/methoxyacetic acid).[20,28,31,33] Propionic acid was used by Wang et al.,[31] but the resulting complex could not be fully characterized. In addition, pivalic acid was introduced by Das et al.[36] but this sterically demanding carboxylate substituent yielded the trinuclear complex $[Co_3(\mu_3\text{–}O)(\mu_2\text{–}OH)(OAc)_5(py)_3]^+$, respectively. Structurally related trinuclear Co-oxo complexes were also previously reported.[14,37]

Studies using mononuclear water oxidation catalysts showed a correlation between catalytic activity and ligand size.[38–41] In addition, the electrochemical properties of $[Co^{III}_4O_4]$ heterocubane-type complexes were tuned by introducing electron-donating/withdrawing ligands, which were found to shift the redox couples cathodically/anodically in the cyclic voltammograms (CV).[28] We therefore became interested in developing a family of Co(III) carboxylate complexes with systematically increased ligand size to improve our knowledge of structure–reactivity relationships. Herein, we report the synthesis and characterization of a series of tetranuclear $[Co_4O_4(O_2CR)_4(py)_4]$ (R = Me **1**, Et **2**, *n*-Pr **3**) and trinuclear Co^{III} complexes $[Co^{III}_3(\mu_3\text{–}O)(\mu_2\text{–}OH)(O_2CR)_3(py)_5](NO_3)_2$ (R = *i*-Pr **4**, *t*-Bu **5**), respectively.

2. Results and Discussion

2.1. Synthesis and Structural Characterization

$[Co_4O_4(O_2CMe)_4(py)_4]$ (**1**), $[Co_4O_4(O_2CEt)_4(py)_4]$ (**2**), and $[Co_4O_4(O_2Cn\text{-}Pr)_4(py)_4]$ (**3**) were synthesized by reactions of $Co(NO_3)_2$ with two equivalents of the corresponding sodium carboxylic acid and pyridine (py) in methanol (MeOH) and H_2O_2 using a slightly modified reaction protocol of Chakrabarty et al.[17] (**Scheme 1**).

Complex **1** was purified by precipitation of a solution of **1** in dichloromethane (CH_2Cl_2, DCM) with petroleum ether and was obtained as a dark green powder. Complexes $[Co_4O_4(O_2CEt)_4(py)_4]$ (**2**) and $[Co_4O_4(O_2Cn\text{-}Pr)_4(py)_4]$ (**3**) were purified by column chromatography using a 2.5:1 mixture of cyclohexane (cHex) and ethanol (EtOH), respectively. The ^{1}H- and ^{13}C nuclear magnetic resonance (NMR) spectra of complexes **1**–**3** (Figure S1, S2, S5, S6, S9, and S10, Supporting Information) show the expected resonances of the carboxylate unit (**Table 1**). Unfortunately, all attempts to further increase the carbon chain length by using the sodium salts of caproic and valeric acids were unsuccessful, since no defined product could be isolated from the resulting resin-like product mixtures. We therefore introduced branched carboxylate ligands by using sodium salts of iso-butyric acid and pivalic acid in order to further increase the steric demand of the carboxylate ligand (**Scheme 2**), resulting in the formation of trinuclear complexes $[Co^{III}_3(\mu_3\text{–}O)(\mu_2\text{–}OH)(O_2CR)_3(py)_5](NO_3)_2$ (R = *i*-Pr **4**, *t*-Bu **5**), respectively.

A pure sample of complex **4** was obtained after washing with tetrahydrofurane (THF). The ^{1}H NMR spectrum of complex **4** (CH_3CN-d^3, Figure S13, Supporting Information) showed resonances of the carboxylate ligand at 2.96 and 2.70 ppm (O_2CCHMe_2, ration of 1:2) and three doublets between 1.05 and 1.15 ppm (O_2CCHMe_2) as well as three resonances for the coordinating

Table 1. ^{1}H- and ^{13}C-NMR resonances [ppm] of the carboxylate ligands in complexes **1**–**3**.

Complex	NMR	OOC	CH_3	CH_2CH_3	$CH_2CH_2CH_3$
1[a)]	^{1}H	–	2.15	–	–
2	^{1}H	–	1.06	2.38	–
3	^{1}H	–	0.88	1.57	2.34
1	^{13}C	188.8	25.6	–	–
2	^{13}C	192.0	9.5	32.6	–
3	^{13}C	191.4	13.3	19.1	41.5

[a)]The ^{1}H resonances of complex **1** (Figure S1, Supporting Information) are systematically shifted to higher field by 0.1 ppm with respect to the resonances reported in the literature[19] due to a different referencing.

$$Co(NO_3)_2 + 2\ NaOOCR + py \xrightarrow[-H_2O,\ -NaNO_3]{\substack{MeOH,\ H_2O_2\\ \Delta T,\ 4\ h}} [Co_4O_4(O_2CR)_4(py)_4]$$

R = Me (**1**), Et (**2**), *n*-Pr (**3**)

Scheme 1. Synthesis of the tetranuclear complexes **1**–**3**.

Research Article
doi.org/10.1002/ejic.202500170

Chemistry Europe
European Chemical Societies Publishing

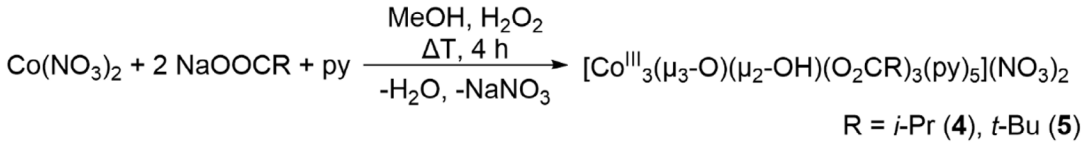

Scheme 2. Synthesis of the trinuclear complexes **4** and **5**.

pyridine ligands in the ratio 1:2:2 with overlapping signals at 8.01 and 7.54 ppm, respectively. In addition, resonances at 1.44 ppm were assigned to the OH protons. Unfortunately, complex **5** always formed as a minor component together with the known complex $[Co^{III}_3(\mu_3\text{–}O)(\mu_2\text{–}OH)(O_2C\textit{t}\text{-}Bu)_5(py)_3]$.[36] Despite several attempts, we failed to isolate complex **5** in its pure form; hence, this compound could not be spectroscopically characterized in detail. However, its crystal structure was determined by single-crystal X-ray diffraction (sc-XRD) using a hand-picked crystal.

2.2. sc-XRD

Single crystals of the known complex **1**, which cocrystallized with five DCM molecules in the unit cell,[14,17,19,21] and the new complexes **2** and **3** suitable for sc-XRD were obtained by slow vapor diffusion of *n*-hexane into solutions of **1**–**3** in DCM. Complexes **2** (**Figure 1**a) and **3** (Figure 1b) crystallize in the monoclinic space group 14 (settings $P2_1/n$ and $P2_1/c$, respectively) with one molecule per asymmetric unit, accompanied by solvent molecules. Central bond lengths and angles of complexes **1**–**3** and of additional tetranuclear complexes with a central $[Co^{III}_4O_4]$ core are summarized in **Table 2**.[14,20,28]

The O and Co atoms alternately occupy the corners of a distorted cube, in which the Co–O–Co bond angles are larger, and the O–Co–O angles are smaller than 90° (see **Table 2**). The arrangement can be described as a Co_4 tetrahedron with μ_3-bridging oxide anions on its faces. Each Co atom is further coordinated by one neutral pyridine ligand, while each carboxylic ligand serves as a μ_2-bridging unit and coordinates to two Co atoms. The Co–O bond lengths within the cubic $[Co^{III}_4O_4]$ core are almost independent from the size of the carboxylic ligand, whereas a steady decrease of the O–Co–O and steady increase

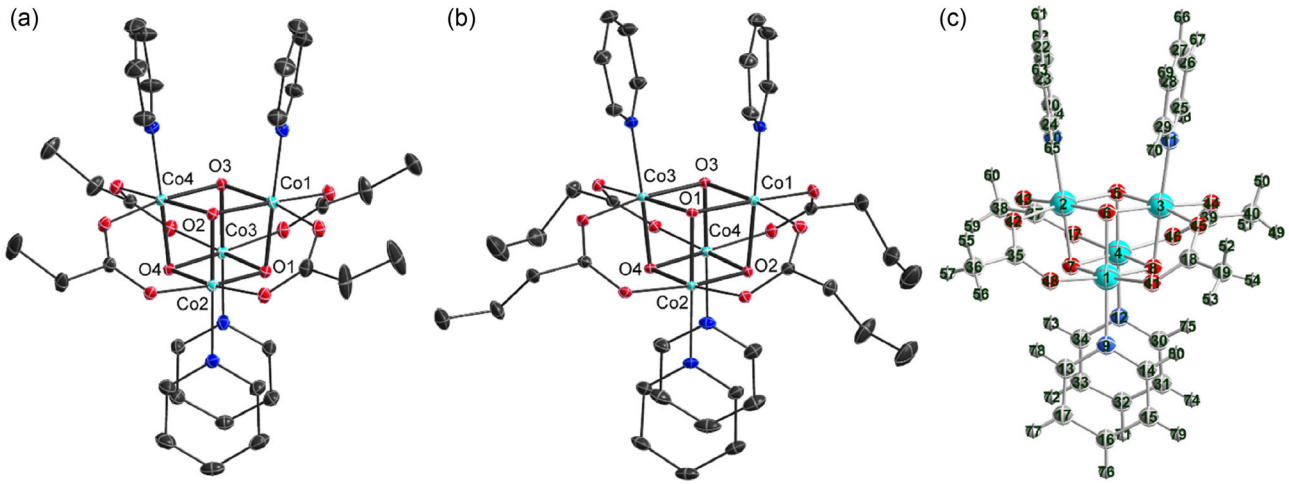

Figure 1. Molecular structures (H atoms not shown) of a) $[Co_4O_4(O_2CEt)_4(py)_4]$ (**2**) and b) $[Co_4O_4(O_2C\textit{n}\text{-}Pr)_4(py)_4]$ (**3**) in the solid state. Displacement ellipsoids are displayed at 50% probability levels. c) Optimized molecular structure of **1** (H atoms shown) including atom numbering at the DFT/PBE0/def2-TZVP level of theory. Color coding: Co light blue; O red; N blue; C gray; and H white.

Table 2. Central bond lengths (Å) and angles (°) within the $[Co_4O_4]$ core of complexes **1**–**3** and of structurally related complexes $[Co_4O_4(O_2CPh)_4(py)_4]$[20] (**I**) and $[Co_4O_4(O_2C_2F_3)_4(py)_4]$[28] (**II**).

Complex	Co-(μ^3–O)	Co–O–Co[a)]	O–Co–O[a)]	Co–N_{Py}	Co–O_{O2C}
1[14]	1.874(2)–1.890(2)	92.35(9)–98.67(10)	81.25(9)–86.99(9)	1.966(3)–1.971(3)	1.955(2)–1.984(2)
2	1.8574(12)–1.8761(12)	91.98(5)–98.38(5)	81.57(5)–87.06(5)	1.9486(14)–1.9647(15)	1.9468(13)–1.9629(12)
3	1.8616(14)–1.8700(15)	92.44(6)–97.94(7)	82.08(6)–87.04(6)	1.9505(18)–1.9590(18)	1.9358(15)–1.9815(15)
I[20]	1.874(4)–1.890(4)	92.35(9)–98.67(10)	81.25(9)–86.99(9)	1.966(4)–1.971(5)	1.955(4)–1.984(4)
II[28]	1.858(2)–1.869(2)	92.98(9)–98.16(9)	81.82(9)–86.42(9)	1.953(3)	1.969(2)–1.979(2)

[a)]Bond angles within the Co_4O_4 core.

Research Article
doi.org/10.1002/ejic.202500170

of the Co–O–Co bond angles within $[Co^{III}_4O_4]$ with increasing steric demand of the carboxylate ligands is observed.

Single crystals of the trinuclear complexes **4** and **5** were obtained by slow vapor diffusion of *n*-hexane into solutions of **4** and **5** in THF. Complexes **4** and **5** crystallize with two nitrate counter ions and one THF solvent molecule per asymmetric unit in monoclinic (**4**, $P2_1/c$) and orthorhombic (**5**, $P2_12_12_1$) space groups, respectively. Additional solvent molecules in **5** could not be modeled and were removed with SQUEEZE.

The central bond lengths within the trinuclear $[Co^{III}_3(\mu_3\text{–}O)(\mu_2\text{–}OH)]$ core and to the coordinating ligands are summarized in **Table 3**. Complexes **4** and **5** are furthermore compared to the known trinuclear complex **III** with $[Co^{III}_3(\mu_3\text{–}O)(\mu_2\text{–}OH)]$ core reported by Sumner et al.[38] No significant differences in bond lengths and angles of the central cores can be found (see **Figure 2**).

2.3. Structure Optimizations

The structure of complex **1** was optimized by quantum chemical calculation using density functional theory (DFT) for the isolated cluster in vacuum (see Figure 1c). Even without symmetry constraints, the structure reveals near S_4 symmetry, allowing for a simple reoptimization in this point group. As symmetry will be important for many comparisons between experiment and theory in the following sections, a few aspects in this regard should be highlighted.

The neat $[Co^{III}_4O_4]^{4+}$ core without ligands, e.g., a hypothetical $[Co_4O_4(O_2CH)_6]^{2-}$ complex containing six formate ($OCHO^-$) ligands would have T_d (tetrahedral) symmetry. Substitution of two of these formate ligands by four linear N-donor ligands like HCN, as in the complex $[Co_4O_4(O_2CH)_4(HCN)_4]$, already reduces the symmetry to D_{2d}. Finally, substitution of the formate by acetate ligands, which lack axial symmetry, and/or HCN by pyridine, which prefers a tilted conformation, reduces the overall symmetry to S_4 for $[Co_4O_4(OAc)_4(py)_4]$ (1). These considerations will be helpful for the understanding of the ultraviolet/visible (UV/vis) and infrared (IR) spectra and their comparisons with spectra for more symmetric model systems (vide infra).

The near tetrahedral symmetry is also reflected in structural parameters such as the Mayer bond indices (MBIs) as calculated here for $[Co_4O_4(OAc)_4(py)_4]$ **1** (see **Table 4**) to characterize the chemical bonding in this complex. In the following discussion, the S_4 axis is assumed to be oriented along the longer, vertical axis, defined as the *z*-axis and in accordance with Figure1c. First, the $[Co^{III}_4O_4]$ core itself is considered. Due to the reduction of the ideal T_d symmetry to S_4, only the atom pairs Co2/Co3 and Co1/Co4 are equivalent, but not necessarily the atoms within these pairs. Thus, there are three sets of Co–Co and Co–O bond lengths. There is moderate covalent Co—O bonding, as indicated by values of ≈0.6. The bond indices for Co2/O5 (0.64) and Co2/O6 (0.63) are almost identical, while that for the Co2/O7 bond (0.60) is marginally smaller, in line with the fact that the $[Co^{III}_4O_4]$ core is slightly stretched along the *z*-axis.

Regarding the structure of the ligands, the MBIs confirm a delocalized three-center π bond (MBI ≈ 1.5) in the carboxylate groups and three mostly equivalent C—H bonds in the methyl group of acetate as well as a local C_{2v} symmetry of pyridine with the typical bond alteration (due to the perturbation by the N atom when compared to benzene). However, analysis of the

Table 3. Central bond lengths [Å]) within the $[Co^{II}I_3(\mu_3\text{–}O)(\mu_2\text{–}OH)]$ core of complexes **4** and **5** as well as the dication $[Co^{III}_3(\mu_3\text{–}O)(\mu_2\text{–}OH)(OAc)_3(py)_5]^{2+}$ (**III.**).[38]

Complex	Co-(μ^3–O)	Co-(μ^2–OH)	Co–N_{Py} [a)]	Co–N_{Py} [b)]	Co–O_{O2C}
4	1.8631(15)–1.8772(15)	1.8858(16)–1.9112(16)	1.953(2)–1.9578(19)	1.9931(19), 2.002(2)	1.8941(16)–1.9156(16)
5	1.8806(18)–1.8903(16)	1.8796(19)–1.9001(19)	1.945(2)–1.964(2)	1.987(2), 1.996(2)	1.8848(19)–1.9121(19)
III[38]	1.862(3)–1.892(4)	1.880(4)–1.906(4)	1.929(5)–1.962(6)	1.983(5), 1.990(4)	1.882(3)–1.909(3)

[a)]Co–N_{Py} distances vertical pyridine in Figure 2. [b)]Co–N_{Py} distances horizontal pyridine in Figure 2.

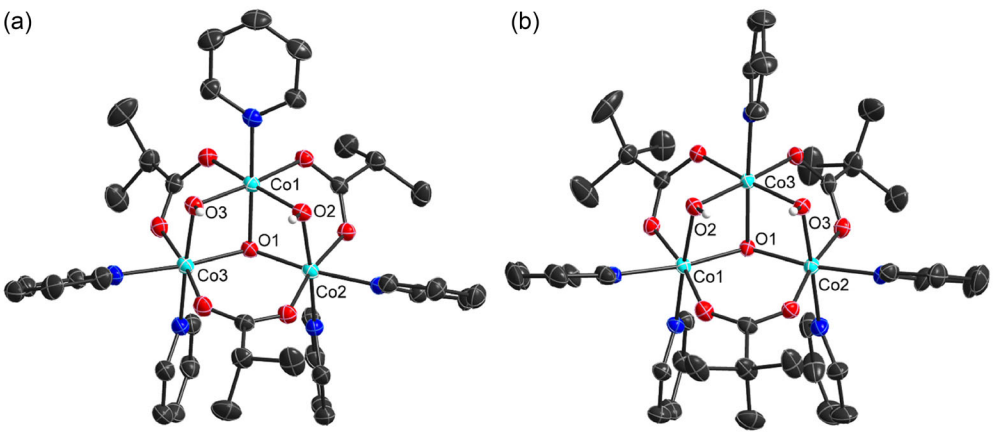

Figure 2. Molecular structures of a) $[Co^{III}_3(\mu_3\text{–}O)(\mu_2\text{–}OH)(O_2C\textit{i}\text{-}Pr)_3(py)_5](NO_3)_2$ (**4**) and b) $[Co^{III}_3(\mu_3\text{–}O)(\mu_2\text{–}OH)(O_2C\textit{t}\text{-}Bu)_3(py)_5](NO_3)_2$ (**5**) in the solid state. Nitrate counter anions, solvent molecule, minor components of disordered parts, and H omitted for clarity except for the OH protons. Color coding: Co light blue; O red; N blue; C gray; and H white. Displacement ellipsoids are displayed at 50% probability levels, H atoms as spheres of arbitrary radii.

Research Article
doi.org/10.1002/ejic.202500170

Table 4. Calculated MBIs for the $[Co^{III}_4O_4]$ core and the acetate and pyridine ligands of complex **1**. Only values for symmetry inequivalent bonds are given. For atom numbering, see Figure 1c.

$[Co^{III}_4O_4]$ core			Acetate			Pyridine		
Atom 1	Atom 2	MBI	Atom 1	Atom 2	MBI	Atom 1	Atom 2	MBI
Co2	O5	0.64	C18	O41	1.53	N10	C24	1.41
Co2	O6	0.63	C18	O45	1.53	C24	C23	1.40
Co2	O7	0.60	C18	C19	0.98	C23	C22	1.43
Co2	N10	0.58	C19	H52	0.97	C22	C21	1.43
Co2	O42	0.50	C19	H53	0.98	C21	C20	1.40
Co2	O43	0.50	C19	H54	0.95	C20	N10	1.39
–	–	–	–	–	–	C24	H65	0.96
–	–	–	–	–	–	C23	H63	0.96
–	–	–	–	–	–	C22	H61	0.96
–	–	–	–	–	–	C21	H62	0.96
–	–	–	–	–	–	C20	H64	0.95

MBIs indicates moderate covalent bonds between Co in the core and the ligands, i.e., to N in pyridine (0.58) and to O in the carboxylate (0.5), presumably with some ionic character.

Due to the similarity of **1** to the larger tetranuclear complexes **2** and **3,** as well as the lower symmetry (C_s) of the trinuclear complexes **4** and **5**, the MBIs of these complexes have not been further investigated. Only exemplarily, some differences in the MBIs of the trinuclear complex **III** (Table S3, Supporting Information) compared to the tetranuclear complex **1** (both with acetate ligands) are worth highlighting. The covalent character of the bonds between the Co atoms and the ligands is increased in **III** (Co—O(acetate) > 0.5; Co—N(pyridine) > 0.6), while that the MBIs for the bonds in the remaining $[Co^{III}_3(\mu_3\text{–}O)(\mu_2\text{–}OH)]$ core (≈ 0.6) are similar to that of $[Co_4O_4]$ without pronounced anisotropy. The O—H bonds of the μ–OH ligands are found to be slightly weakened compared to an isolated OH^- (0.87).

2.4. Stability Analysis

Since the synthesis of tetranuclear complexes with branched carboxylate ligands remained unsuccessful, the relative stability of the tetranuclear versus trinuclear complexes has been analyzed using DFT calculations. We consider the conversion of the trinuclear $[Co_3O(OH)_2]$ into the tetranuclear $[Co_4O_4]$ species according to

$$4\ [Co^{+III}_3(\mu_3-O)(\mu_2-OH)_2(O_2CR)_3(L)_5]^{2+} \rightleftharpoons 3\ [Co^{+III}_4(\mu_3-O)_4(O_2CR)_4(L)_4] + 8\ L + 8\ H^+ \quad (1)$$

whose Gibbs free energy (in solution) is given by

$$\Delta G(R) = 3G(Co_4O_4;R) + 8G(L) + 8G(H^+) - 4G(Co_3O(OH)_2;R) \quad (2)$$

written as a function of the group R at the carboxylate (O_2CR). Thus, comparing the reaction energy for complexes with two different carboxylates (R_1, R_2), the difference in reaction energy becomes

$$\begin{aligned}\Delta(\Delta G) &= \Delta G(R_2) - \Delta G(R_1) \\ &= 3\ [G(Co_4O_4;R_2) - G(Co_4O_4;R_1)] - 4\ [G(Co_3O(OH)_2;R_2) \\ &\quad - G(Co_3O(OH)_2;R_1)]\end{aligned} \quad (3)$$

depending only on the total Gibbs free energies of the $[Co_3O(OH)_2]$ and $[Co_4O_4]$ species but not the free (pyridine) ligand L or H^+.

As can be seen in **Table 5**, the position of the trinuclear ($[Co^{III}_3(\mu_3\text{–}O)(\mu_2\text{–}OH)]$) versus tetranuclear ($[Co_4O_4]$) equilibrium lies in the case of acetate (R = Me) relative to formate (R = H) more than 100 kJ mol^{-1} on the tetranuclear site in the polar solvent methanol (MeOH). Increasing the steric demand at the carboxylate group by using *iso*-butyrate (R = *i*-Pr) results in a shift of the equilibrium position by ≈50 kJ mol^{-1} toward the trinuclear complex, and further increase of the steric demand (R = *t*-Bu, pivalate) results in an additional shift of ≈13 kJ mol^{-1}. The calculations demonstrate the relative destabilization of the tetranuclear species by increasing the steric demand of the carboxylate ligand, facilitating the formation of the trinuclear species. This trend is also more pronounced when pyridine is replaced by HCN as a model ligand, since the Δ*G* value becomes even positive for R = *t*-Bu relative to R = H (see Table S4, Supporting Information).

Table 5. Relative Gibbs free energies in solution (kJ mol^{-1}) for the interconversion from a trinuclear ($[Co^{III}_3(\mu_3\text{–}O)(\mu_2\text{–}OH)(O_2CR)_3(py)_5]^{2+}$) into a tetranuclear ($[Co_4O_4(O_2CR)_4(py)_4]$) complex according to Equation (3) for different carboxylate ligands (O_2CR) relative to formate (R = H) in methanol. Please notice that the values in other solvents differ (see Table S4, Supporting Information, for Et_2O, THF, and cyclohexane).

R	Complex	Relative stability [kJ mol^{-1}]
H	–	0
Me	III	−103
i-Pr	4	−51
t-Bu	5	−38

Research Article
doi.org/10.1002/ejic.202500170

2.5. Spectroscopic Characterization

The IR spectra of the complexes **1**–**3** (Figure S3, S7, and S11, Supporting Information) are almost identical. All complexes exhibit four intense absorption bands below 800 cm^{-1} in accordance with comparable complexes, which also possess four intense IR absorption bands (≈760–570 cm^{-1}).[17] While the absorption band at ≈760 cm^{-1} results from ring-based vibrations of the pyridine ring, the other three intense bands are tentatively assigned to characteristic vibrations of the heterocubane-type $[Co^{III}_4O_4]$ core. The band at ≈630 cm^{-1} represents the typical Co–O stretching vibration[17] and was also observed in structurally related trinuclear $M_3(\mu_3\text{–}O)$ (with M = Co or Mn) complexes[42] as well as in a comparable Mn_4O_4 complex.[43]

We also used DFT to compute the IR absorption spectrum of **1** in vacuum. A comparison of the experimental IR spectra in acetonitrile solution (CH_3CN) and solid state (crystal) shows a good agreement with respect to the peak positions of the different vibrational modes (**Figure 3**). However, the intensity of the two dominant bands around 1500 cm^{-1} was found to decrease relative to the intensity of the signals in the 500–1000 cm^{-1} region in the solid state compared to solution. This difference in the intensity ratios hints toward packing effects in the solid phase, preventing volume-expensive molecular vibrations, which is also in line with the opposite intensity ratios of these groups of signals in the calculated IR spectrum (in vacuum). Still, these main features can be said to be qualitatively reproduced by the calculations (vide infra).

The calculated IR spectrum successfully reproduces the main characteristic and most intense features of the experimental spectrum (Figure 3), i.e., the $[Co^{III}_4O_4]$ signals (500–1000 cm^{-1}) and the two intense groups around 1500 cm^{-1}. Despite a clear spectral shift between the calculated and experimental spectra, no attempts of scaling the harmonic frequencies have been undertaken. This shift and the missing signals in higher wavenumbers can be partly explained due to the nature of the attenuated total reflectance-infrared (ATR-IR) method. In contrast to classical transmission IR, the ATR-IR method depends on the refractive index. This leads to a dependence of the intensity and shift of the IR signals on the latter. In ATR-IR, the peak intensities and width increase with decreasing wavenumbers.[44]

Normal mode analysis of the vibrations allows us to dissect the total IR absorption spectrum of **1** into different contributions (**Figure 4**). Main signals in the region above 3000 cm^{-1} originate from the aromatic C–H stretching vibrations of the pyridine ligands (3070/3170/3210/3250 cm^{-1}), with the signals of the aliphatic C–H stretches from the CH_3 group of the acetate ligand (3000 cm^{-1}) being subordinate. In contrast, the region between 1000 and 2000 cm^{-1} is dominated by the symmetry-allowed combinations of the symmetric (1500 cm^{-1}) and asymmetric (1680/1700 cm^{-1}) C–O stretching vibrations of the carboxylate groups in the acetates, in good agreement with the experimental spectra.

The region below 1000 cm^{-1}, particularly between 500 and 1000 cm^{-1}, is most interesting as it contains the characteristic signals from the $[Co^{III}_4O_4]$ core. Whereas the total spectrum in this region has five apparent main bands (≈610/650/680/720/785 cm^{-1}), only two of these can be ascribed to the $[Co^{III}_4O_4]$ core. The first band around 610 cm^{-1} consists of a twofold degenerate *E* mode at 606 cm^{-1} and a *B* mode at 612 cm^{-1} (Table S5, Supporting Information), while the second band at 680 cm^{-1} consists of an *E* mode at 681 cm^{-1} and a *B* mode at 687 cm^{-1}; originating from twisting/bending and wagging motions of the $[Co^{III}_4O_4]$ core. In particular, a comparison with additional model systems with higher symmetry (Figure S17, Supporting Information) showed that these two groups of signals would ideally belong to a dipole-allowed triply degenerate T_2 mode in the T_d point group. The other signals at 650 and 710 cm^{-1} refer to 1) a collective motion and 2) two individual, energetically close vibrations of the pyridine and acetate ligands, respectively. A detailed assignment of the 12 main localized vibrational modes and a comparison with the $[Co_4O_4(O_2CH)_4(HCN)_4]$ (D_{2d}) and $[Co_4O_4(O_2CH)_6]^{2-}$ (T_d) model systems is given in Table S2, Supporting Information. In direct comparison with the experiments (Figure 3), the bands in the calculated spectra appear to be shifted by about 30–40 cm^{-1} in this region. The two signals of the pyridine ligands are reproduced (720/785 cm^{-1}), while the frequency splitting between the *B* and *E* contributions of the

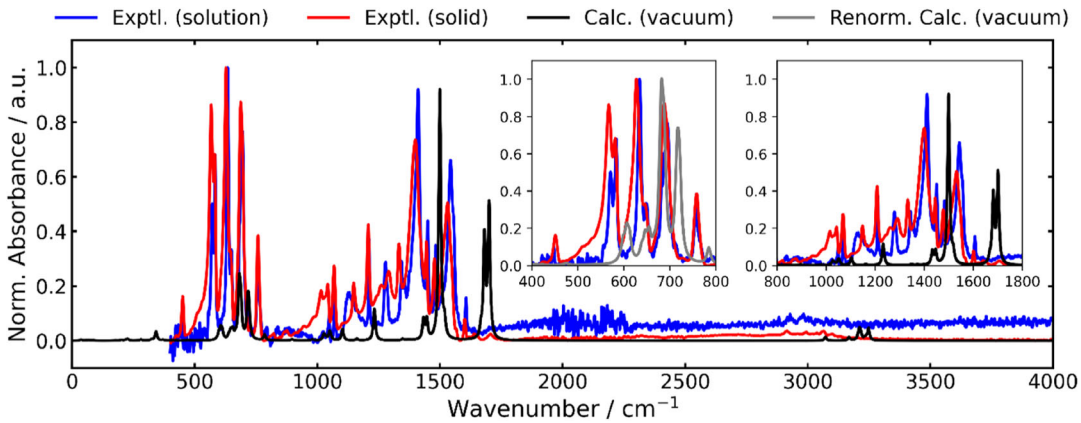

Figure 3. Comparison of the experimental IR absorption spectra in the solid (crystal) and solution (acetonitrile) phase and the calculated harmonic vibrational spectrum of **1** (S_4 symmetry) in vacuum at the tight PBE0/def2-TZVP level of theory.

Research Article
doi.org/10.1002/ejic.202500170

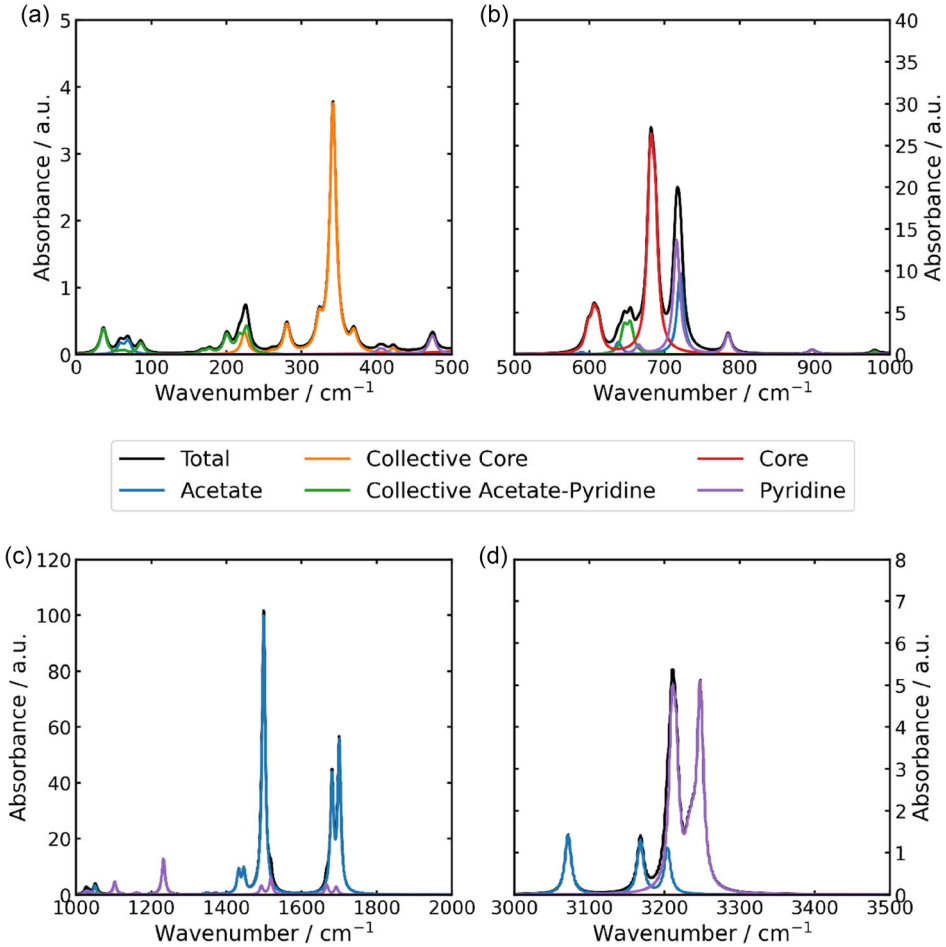

Figure 4. Decomposition of the calculated vacuum IR absorption spectrum of **1** into contributions from the ligands and the Co-oxo core.

$[Co^{III}_4O_4]$ core modes appears to be larger in the experimental spectra. Besides, the collective mode of the acetate and pyridine ligands appears to be missing in the experimental spectra, presumably due to packing effects that suppress this mode and lower its transition dipole moment. Finally, the only relatively intense signal in the region below 500 cm^{-1} refers to a collective vibration of the core and its ligands.

The experimental and calculated IR spectra of the trinuclear complex **4** (Figure S18, Supporting Information) also agree well. The most intense features in the experimental spectrum below 2000 cm^{-1} (e.g., the symmetric and asymmetric carbonyl stretching) are reproduced well despite small shifts and different intensity ratios, as was observed for complex **1**. We also performed an analysis to dissect the vibrational spectrum into different contributions from the ligands and the core (Figure S19, Supporting Information). Signals corresponding to the carboxylate and pyridine ligands are, unsurprisingly, very similar to those of complex **1**. In contrast, complex **4** is expected to show a high-frequency O–H stretch mode above 3000 cm^{-1}. Most interesting are the differences in the 500–1000 cm^{-1} region, where the characteristic contributions from the $[Co^{III}_3(\mu_3\text{–}O)(\mu_2\text{–}OH)]$ core are located. Compared to the tetranuclear complex **1**, the trinuclear complex **4** reveals a more complex structure with (at least) nine (550/600/650/685/720/740/790/870/950 cm^{-1}) instead of five apparent bands. Only six of these bands are characteristic of the Co-oxo core, while the signals at 650 cm^{-1} (carboxylate) and 720/790 cm^{-1} (pyridine) stem from the ligands. The trinuclear $[Co^{III}_3(\mu_3\text{–}O)(\mu_2\text{–}OH)]$ core differs from being just a corner of the $[Co_4O_4]$ core due to protonation of two μ_3–O groups to μ–OH groups and a higher ratio of pyridine to carboxylate ligands. The resulting lower symmetry leads to a splitting of the signals. The three absorption bands with the highest frequency (740/870/950 cm^{-1}) originate from symmetric and asymmetric bending modes of the μ–OH ligand, and the wagging vibration at 550 cm^{-1} also has large contributions from the μ–OH ligand. Characteristic for the central μ_3–O atom is the vibrations at 600 and 685 cm^{-1}, which are also observed for the tetranuclear complex **1**. A detailed assignment of the vibrational modes characteristic of the $[Co^{III}_3(\mu_3\text{–}O)(\mu_2\text{–}OH)]$ core is given in Table S6, Supporting Information.

The experimental UV/vis absorption spectra of **1** in acetonitrile (Figure S4, Supporting Information) reveal three characteristic features: 1) a very weak $\varepsilon_{630\ nm} = 0.042 \frac{L}{mmol \times cm}$ shoulder around 630 nm, 2) a more intense peak $\varepsilon_{362\ nm} = 0.874 \frac{L}{mmol \times cm}$ at ≈362 nm, and 3) a very intense $\varepsilon_{253\ nm} = 2.088 \frac{L}{mmol \times cm}$ signal below 253 nm. Time-dependent density functional theory

Research Article
doi.org/10.1002/ejic.202500170

(TDDFT) calculations reproduced features (1) and (2) but failed for feature (3).

The calculations reveal a set of lowest-energy transitions with weak oscillator strengths (f): from the (totally symmetric) singlet ground ($X = 1\ ^1A$) state into the 1 ^1E state at 607 nm (2.04 eV, $f = 2 \times 10^{-3}$), the 2 ^1E state at 576 nm (2.15 eV, $f = 0.2 \times 10^{-3}$), and the 3 ^1E state at 562 nm (2.21 eV, $f = 0.3 \times 10^{-3}$). According to the natural transition orbitals (NTOs) in **Figure 5** and S21–S22, Supporting Information, these transitions can be characterized as d–d transitions, in line with the previous assignment of feature (1) at 630 nm in the experimental spectrum.[17,19] Moreover, a second, similarly weak transition into the 4 ^1B state around 419 nm (2.96 eV, $f = 2 \times 10^{-3}$) with d/p–d/p character (Figure S23, Supporting Information) appears in the experimental spectrum as an additional shoulder around 500 nm. Lastly, signal (2) from the experimental spectrum at 370 nm can be assigned to a metal-to-ligand charge-transfer (MLCT) transition, corresponding to the 8 ^1B state (284 nm, 4.40 eV, $f = 0.1$), which fits well to the postulated MLCTs of the μ_3–O–Co^{III} (355 nm) and the carboxylate–O–Co^{III} unit (250 nm),[19] respectively. The corresponding NTOs are shown in **Figure 6**. This assignment of the experimental features (1) and (2) has further been verified by an additional comparison with model systems (Figure S24, Supporting Information), demonstrating that the rather intense d–d transitions, including feature (1), are not affected by the solvent or the carboxylate ligand, but change with the N-donor ligand. In contrast, the MLCT state does show a blue shift and is absent if the pyridine ligand is replaced by the simple HCN ligand.

2.6. Electrochemica Properties

A few studies have been devoted to the synthesis and catalytic application of tetranuclear heterocubane-type complexes containing a $[Co^{III}_4O_4]$ core; however, data on their redox properties, despite their importance for catalysis, are largely lacking. It has been reported that the redox potentials of such tetranuclear complexes are directly correlated to their ligand environment.[28] We therefore investigated the influence of the carboxylate ligand size on the redox properties of complexes **1**–**3**. The CV of complexes **1**–**3** are shown in Figure 6a over the potential range of 0–1.68 V versus Fc/Fc^+ and in the narrower potential range around peak E1 in Figure 6b. All complexes revealed two (quasi)reversible redox peaks: E1 centered at 0.3 V, which can be assigned to the $[Co^{III}_4O_4]^{4+}/[Co^{IV}Co^{III}_3O_4]^{5+}$ couple, and E2 at around 1.4 V, which can be assigned to the $[Co^{IV}Co^{III}_3O_4]^{5+}/[Co^{IV}_2Co^{III}_2O_4]^{6+}$ couple, in agreement with literature values.[28] This suggests that the oxidation of the $[Co^{III}_4O_4]$ core gives access to Co^{IV}-oxo intermediates; however, the charge is expected to be delocalized over all cobalt atoms. These higher oxidation states of metals are discussed in many catalytic OER cycles at Co_3O_4 spinel catalysts,[9,45] demonstrating that tetranuclear heterocubane-type complexes with a $[Co^{III}_4O_4]$ core can indeed serve as a functional mimic of

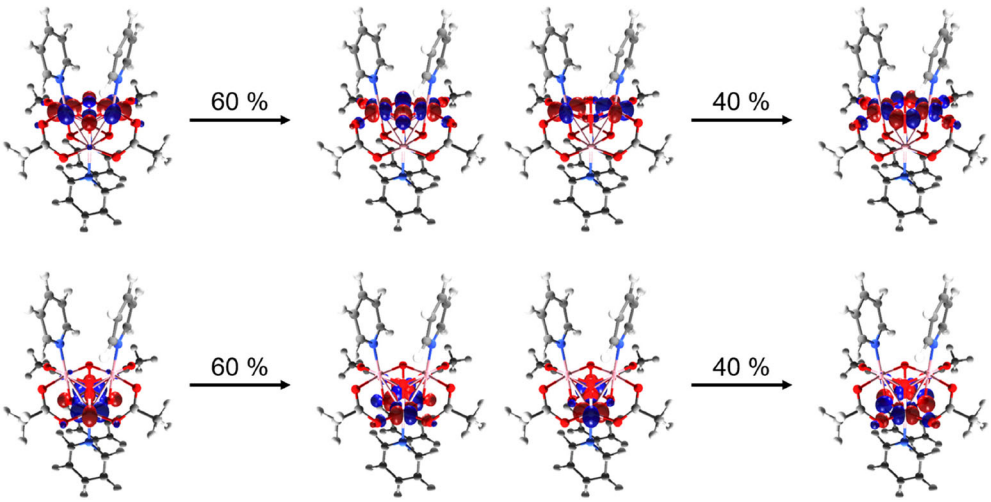

Figure 5. NTOs for the two transitions into the degenerate 1 ^1E state with d–d character.

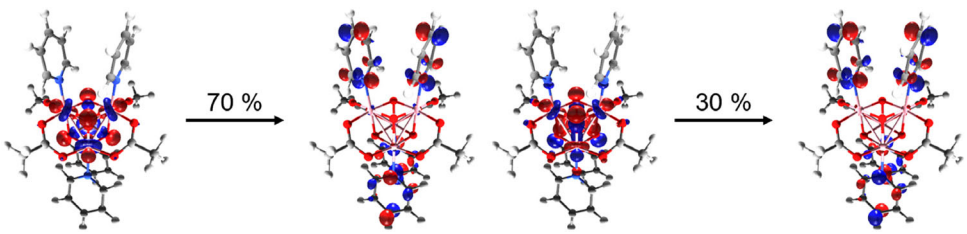

Figure 6. NTOs for the transition into the 8 ^1B state with MLCT character.

Research Article
doi.org/10.1002/ejic.202500170

heterogeneous spinel-type Co_3O_4 OER catalysts. We interpret the small hump at 0.85 V in the anodic scan as ligand oxidation, in accordance with the literature.[46]

Interestingly, the redox potentials of E1 and E2 were slightly but steadily shifted to lower potentials with increasing length of the alkyl chain of the carboxylate ligand, as presented in the correlation plot shown in the inset of **Figure 7**b. The formal redox potential of peak E1 for complexes **1**, **2,** and **3** was 0.324, 0.311, and 0.294 V versus Fc/Fc^+, respectively. This trend of lowering the redox potential by lengthening the alkyl chain may be related to differences in the solvent effect and the stabilization of charged species. We note that the redox shift is rather small, which is expected as the change in the ligand size is just from $-CH_2$ to $-CH_2CH_2CH_3$ and not a substantial substitution or branching of the ligand. Furthermore, the effect of the scan rate on the redox behavior of oxo-cubanes was studied, as presented in Figure S26, Supporting Information. Data were analyzed by plotting the peak current (I_p) versus the square root of the scan rate ($v^{1/2}$) (Randles–Sevcik plot). The graphs (Figure S26d, Supporting Information) showed excellent linearity with R^2 of 0.9999, suggesting a diffusion-limited process. The plots are almost identical for the three different complexes, which is anticipated for a small change in the molecular size of the complexes. The diffusion coefficient (D) was estimated using Randles–Sevcik analysis, and the obtained average diffusion coefficient (D) of the three complexes in tetrabutylammonium hexafluorophosphate ($TBAPF_6$)/MeCN electrolyte is $(7.5 \pm 0.3) \times 10^{-6}\ cm^2\ s^{-1}$.

In addition, the electrochemical behavior of the trinuclear complex **4** was studied by CV (Figure S27a, Supporting Information). Within the same investigated potential range, the CV of complex **4** shows a different voltammetric behavior from the tetranuclear cubane complexes, e.g., complex **1**, where only an irreversible oxidation peak occurs at about 1.41 V versus Fc/Fc^+, close to the potential of the second oxidation peak of complex **1**. However, in a larger potential window, the CV of complex **4** shows additional oxidation and reduction peaks (Figure S27b, Supporting Information). From studying different potential windows, one can correlate the reduction peak C2 to oxidation peak A2, while C1 is related to A1. Peaks A1 and A2 can be attributed to oxidation of Co(III) to Co(IV), and peaks C1 and C2 are probably due to reduction to Co(III) and possibly even to Co(II). Similar interpretation, though for different peak potentials, was reported for other Co complexes.[47,48] Moreover, the peak potential was shifted with increasing the scan rate, suggesting a kinetically controlled irreversible process (Figure S27c, Supporting Information). To this end, such structure–reactivity correlations can provide a guide for the rational design of oxo-cubanes and open a new avenue for accessing higher oxidation state Co(IV) intermediate, which can be highly active for catalyzing reactions such as OER.

3. Conclusions

A series of neutral tetranuclear Co(III) carboxylate complexes $[Co_4O_4(O_2CR)_4(py)_4]$ (R = Me **1**, Et **2**, *n*-Pr **3**) with a central heterocubane-type $[Co^{III}{}_4O_4]$ core as well as trinuclear complexes $[Co^{III}{}_3(\mu_3\text{–}O)(\mu_2\text{–}OH)(O_2CR)_3(py)_5](NO_3)_2$ (R = *i*-Pr **4**, *t*-Bu **5**) with a central dicationic $[Co^{III}{}_3(\mu_3\text{–}O)(\mu_2\text{–}OH)]$ core were synthesized and spectroscopically characterized (^{1}H-,^{13}C-NMR and Fourier transform-infrared (FT-IR)), while their structures in the solid state were determined by sc-XRD. The gas phase structure of $[Co_4O_4(OAc)_4(py)_4]$ (**1**) was determined by use of quantum chemical calculations, and MBIs were calculated to investigate the electronic structure of **1** in more detail. The DFT simulated IR spectrum of **1** agrees well with the experimental spectrum and allows for a distinctive assignment of the ligand-based and Co-oxo-based modes. Electronic transitions in the tetranuclear complexes, as determined using UV/vis spectroscopy, are consistent with computational results based DFT. Furthermore, the electrochemical properties of complex **1**–**4** are compared. CV measurements revealed (quasi)reversible redox peaks of all complexes with slightly decreasing redox potentials with increasing carbon chain length of the ligand, and the isolation and structural characterization of as-formed oxidation products is currently under investigation.

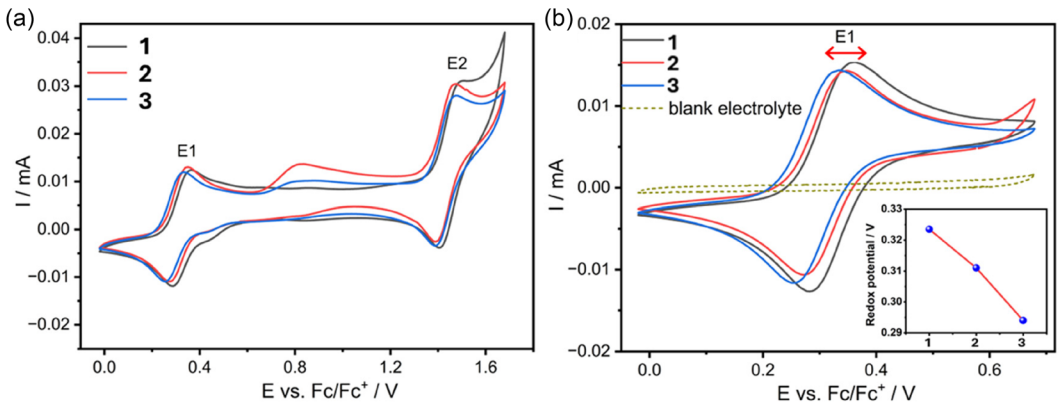

Figure 7. CV of 1 mM cubane complex in 0.1 M $TBAPF_6$/MeCN obtained at a GC electrode at 100 mVs^{-1} over a) wider and b) shorter potential window. Inset: variation of the formal redox potential of E1 for different complexes. The potential was normalized against the Fc/Fc^+ internal redox couple.

Research Article
doi.org/10.1002/ejic.202500170

4. Experimental Section

Materials and Reagents

All reagents were commercially available and used without further purification. Synthesis of all complexes followed a modified procedure of Chakrabarty et al.[17]

Synthesis of Complexes 1–5

$[Co_4O_4(OAc)_4(py)_4]$ (1): $Co(NO_3)_2.6H_2O$ (10 mmol, 2.9 g) and NaOAc (20 mmol, 1.6 g) were dissolved in 30 mL of MeOH. After heating the solution to reflux, pyridine (10 mmol, 0.8 mL) and 30% H_2O_2 (50 mmol, 5 mL) were slowly added, and the purple mixture immediately turned dark green. The solution was heated to reflux for an additional 4 h. After half of the solvent was removed at reduced pressure, 20 mL of DCM was added. The resulting dark green organic phase was collected and dried with $MgSO_4$. Half of the solvent was then removed at reduced pressure, and the product was precipitated with petroleum ether. After drying at reduced pressure, a dark green powder was obtained. Single crystals were grown by slow evaporation of the solvent from a solution of **1** in DCM. Yield: 77% based on Cobalt. Anal. calcd. for $C_{28}H_{32}O_{12}N_4Co_4$ (852 g mol^{-1}) C: 39.46%; H: 3.78%; N: 6.57%; Co: 27.66%. Found: C: 38.8%; H: 3.84%; N: 6.64%; Co: 28.1%. ^{1}H NMR (400 MHz, D_2O) δ 8.27 (d, $^3J_{H-H} = 5.2$ Hz, 8 H, py o-H), 7.80 (m, 4 H, py p-H), 7.29 (dd, $^3J_{H-H} = 7.6$; $^3J_{H-H} = 6.5$ Hz, 8 H, py m-H), 2.30–1.99 (s, 12 H, $OOCH_3$). ^{13}C NMR (101 MHz, D_2O) δ 188.84 (s, OOC), 151.99 (s, py o-C), 138.94 (s, py p-C), 124.88 (s, py m-C), 25.60 (s, CH_3).

$[Co_4O_4(O_2CEt)_4(py)_4]$ (2): The synthesis was performed similar to that of **1**, but replacing NaOAc by NaO_2CEt (20 mmol, 1.924 g). Since **2** did not precipitate after the addition of petroleum ether, **2** was purified by column chromatography (silica column) and a mixture of cHex/EtOH (2.5:1). The first fraction was collected, and after removing the solvent at reduced pressure, a dark green powder was obtained. Single crystals were obtained by vapor diffusion of *n*-hexane into a solution of **2** in DCM. Yield: 45.5% based on Cobalt. Anal. calcd. for $C_{32}H_{40}O_{12}N_4Co_4$ (908 g mol^{-1}) C: 42.31%; H: 4.44%; N: 6.17%; Co: 25.95%. Found: C: 41.71%; H: 4.59%; N: 5.98%; Co: 26.4%. ^{1}H NMR (400 MHz, D_2O) δ 8.28 (dd, $^3J_{H-H} = 6.3$; $^4J_{H-H} = 1.3$ Hz, 8 H, py o-H), 7.80–7.74 (m, 4 H, py p-H), 7.27 (dd, $^3J_{H-H} = 7.6$; $^3J_{H-H} = 6.5$ Hz, 8 H, py m-H), 2.47–2.31 (q, $^3J_{H-H} = 7.5$ Hz, 8 H, CH_2), 1.06 (t, $^3J_{H-H} = 7.6$ Hz, 12 H, CH_3). ^{13}C NMR (101 MHz, D_2O) δ 191.97 (s, OOC), 152.07 (s, py o-C), 138.79 (s, py p-C), 124.79 (s, py m-C), 32.57 (s, CH_2), 9.52 (s, CH_3).

$[Co_4O_4(O_2Cn\text{-}Pr)_4(py)_4]$ (3): The synthesis was analogously performed with NaO_2CPr (20 mmol, 2.255 g), resulting in the isolation of a dark green powder. Single crystals were obtained by vapor diffusion of *n*-hexane into a solution of **3** in DCM. Yield: 9.3% based on Cobalt. Anal. calcd. for $C_{36}H_{48}O_{12}N_4Co_4$ (964 g mol^{-1}) C: 44.83%; H: 5.02%; N: 5.81%; Co: 24.44%. Found: C: 44.81%; H: 5.24%; N: 5.66%; Co: 24.73%. ^{1}H NMR (400 MHz, D_2O) δ 8.29 (dd, $^3J_{H-H} = 6.4$ Hz; $^4J_{H-H} = 1.4$ Hz 8 H, py o-H), 7.77 (tt, $^3J_{H-H} = 7.7$ Hz; $^4J_{H-H} = 1.5$ Hz 4 H, py p-H), 7.27 (dd, $^3J_{H-H} = 7.6$; $^3J_{H-H}$ 6.5 Hz, 8 H, py m-H), 2.38–2.30 (m, 8 H, $OOCCH_2$), 1.57 (m, 8 H, CH_2), 0.91–0.86 (t, $^3J_{H-H} = 7.4$ Hz, 12 H, CH_3). ^{13}C NMR (101 MHz, D_2O) δ 191.38 (s, OOC), 152.19 (s, py o-C), 138.84 (s, py p-C), 124.82 (s, py m-C), 41.51 (s, $OOCCH_2$), 19.07 (s, CH_2CH_3), 13.32 (s, CH_3).

$[Co^{III}_3(\mu_3\text{–}O)(\mu_2\text{–}OH)_2(O_2Ci\text{-}Pr)_3(py)_5]^{2+}$ $2NO_3^-$ (4): The synthesis was performed similar to that of **1,** but replacing NaOAc by NaO_2Ci-Pr (20 mmol, 2.200 g). Since **4** did not precipitate after the addition of petroleum ether or cHex, **4** was purified by washing with THF. Resulting in the isolation of a dark green powder. Single crystals were obtained by vapor diffusion of *n*-hexane into a solution of **4** in THF. Yield: 2.37% based on Cobalt. Anal. calcd. for $C_{35}H_{52}O_{13}N_3Co_3$ (899,61 g mol^{-1}) C: 46.73%; H: 5.83%; N: 4.67%; Co: 19.65%. Found: C: 44.00%; H: 5.68%; N: 4.42%; Co: 20.70%. ^{1}H NMR (400 MHz, CD_3CN) δ 8.52 (dd, $^3J_{H-H} = 6.4$; $^4J_{H-H} = 1.3$ Hz, 2H, py o-H), 8.43 (d, $^3J_{H-H} = 5.2$ Hz, 4 H, py o-H), 8.05–7.95 (m, 3H, 2 py p-H), 7.88 (s, 4H, py o-H), 7.63 (t, $^3J_{H-H} = 7.6$ Hz, 2 H, py p-H), 7.58–7.51 (m, 6H, 2 py m-H), 7.15 (t, $^3J_{H-H} = 6.9$ Hz, 4 H), 2.96 (hept, $^3J_{H-H} = 7.0$ Hz, 1H, OOCCH), 2.70 (hept, $^3J_{H-H} = 7.0$ Hz, 2H, OOCCH), 1.43 (s 2 H, OH) 1.15 (d, $^3J_{H-H} = 7.0$ Hz, 6 H, CH_3), 1.10 (d, $^3J_{H-H} = 7.0$ Hz, 6H, CH_3), 1.05 (d, $^3J_{H-H} = 6.9$ Hz, 6 H, CH_3). ^{13}C NMR (101 MHz, CD_3CN) δ 195.07 (s, OOC), 193.70 (s, OOC), 153.36 (s, py o-C), 153.09 (s, py o-C), 152.54 (s, py o-C), 140.51 (s, py p-C), 140.26 (s, py p-C), 125.93 (s, py m-C), 125.66 (s, py m-C), 38.89 (s, CH), 38.01 (s, CH), 19.83 (s, CH_3), 19.61 (s, CH_3), 19.55 (s, CH_3).

$[Co^{III}_3(\mu_3\text{–}O)(\mu_2\text{–}OH)_2(O_2Ct\text{-}Bu)_3(py)_5]^{2+}$ $2NO_3^-$ (5): The synthesis was performed similar to that of **1**, but replacing NaOAc by NaO_2Ct-Bu (16.5 mmol, 2.050 g). Single crystals were obtained by slow vapor diffusion of *n*-hexane into a solution of **5** in THF. Complex **5** only formed as minor product in all experiments, while the major component turned out to be the known complex $[Co^{III}_3(\mu_3\text{–}O)(\mu_2\text{–}OH)(OOCt\text{-}Bu)_5(py)_3]^+$ NO_3^- initially reported by Das et al.[36]

Spectroscopic Characterization

IR spectra were collected on a Bruker ALPHA-P FT-IR with a single reflection ATR sample head. IR measurements were performed in a glovebox under argon atmosphere. UV/vis spectra were recorded on a Shimadzu UV-2600i spectrophotometer.

Electrochemical Measurements

CV measurements were conducted using an Autolab PGSTAT204 potentiostat/galvanostat in a three-electrode setup comprising a glassy carbon (GC) (3 mm diameter) working electrode, Pt sheet as the counter electrode, and Ag/AgCl (3M KCl) as the reference electrode. Prior to recording CVs, the GC electrode was polished with alumina slurry (3.0, 1.0, and 0.05 μm in a descending order) on lapping cloths (Buehler, USA). The electrodes were then rinsed with acetone and water and dried under air flow. The potentials were converted to a scale versus Fc/Fc^+, where its formal potential was experimentally determined in the same studied electrolyte.

sc-XRD

Crystals were mounted on nylon loops in inert oil. Data were collected on a Bruker AXS D8 Kappa diffractometer with APEX2 detector (mono-chromated $Mo_{K\alpha}$ radiation, $\lambda = 0.71073$ Å) at 100(2) K. Those of **4** were collected on a Bruker AXS D8 Venture diffractometer with Photon II detector (monochromated $Cu_{K\alpha}$ radiation, $\lambda = 1.54178$ Å, mircofocus source) at 100(2) K. The structures were solved by direct methods (SHELXS-2013)[49] and refined anisotropically by full-matrix least-squares on F^2 (SHELXL-2017).[50,51] Absorption corrections were performed semiempirically from equivalent reflections on basis of multiscans (Bruker AXS APEX3). Hydrogen atoms were refined using a riding model or rigid methyl groups.

The OH hydrogen atom in **2** was refined freely with its O–H bond lengths restrained to be equal to 0.85 Å (DFIX). In **2** and **4**, the OH hydrogen atoms' displacement parameters were coupled to the ones of the corresponding O, while those in **5** were refined freely without any con- or restraints.

The structure of **2** contains two dichloromethane molecules, of which one is disordered over two sites. The Cl–Cl bond lengths and Cl–C–Cl angles were restrained to be equal (SADI), and RIGU restrained were used in the refinement of the displacement parameters. A methanol

Research Article
doi.org/10.1002/ejic.202500170

and an *n*-pentane molecule are disordered over a center of inversion. The local symmetry was ignored in the refinement of the pentane (negative PART). The bond lengths and angles of the pentane molecule were restrained to be equal (SADI). Its displacement parameters were constrained to be equal and equal to those of the carbon atom of the methanol, which is in close proximity (EADP) and strongly correlated. In addition, an ethyl group is disordered over two positions. The crystal was twinned, and the model was refined as a two-component pseudo-merohedral twin (TWIN, BASF). A separate integration of the components failed due to overlapping. Despite the small contribution of the minor component (≈3%), the *R*-values are significantly reduced.

In **3**, a dichloromethane molecule is disordered over two positions. Due to the close proximity, the alternate positions of the atoms were refined with common displacement parameters (EADP). The displacement ellipsoids of the other solvent molecule suggest minor disorder, but a refinement with split positions failed. During the measurement, ice formed on the crystals, and the resulting diffraction may have distorted individual reflection intensities.

An anion and the solvent molecule of **4** are disordered. They could be crudely modeled by two alternate positions; however, their displacement parameters suggest further disorder, which could not be resolved. The corresponding bond lengths and angles were restrained to be equal (SADI), and RIGU restraints were applied to the displacement parameters. In case of the nitrate, additional SIMU restraints were used, and due to their close proximity, the nitrogens' displacement parameters were constrained to be equal (EADP).

In **5**, a *t*-butyl group and a nitrate are disordered over two positions. The bond lengths and angles of all nitrate ions were restrained to be equal, and RIGU restraints were applied to their displacement parameters. Due to their close proximity, the displacement parameters of N1_1 and N1_7 were constrained to be equal (EADP). The corresponding bond lengths and angles of the solvent molecules were restrained to be equal (SADI), and RIGU and SIMU restraints were applied to their displacement parameters. Three of them were too disordered to be modeled properly. The final refinement of the model was done against a dataset from a PLATON/SQUEEZE run were these molecules had been removed.[52] The molecules were included in the sum formula for completeness. The model was refined as a two-component inversion twin.

CCDC-2392548 (**2**), -2392549 (**3**) -2430856 (**4**), and -2430857 (**5**) contain the supplementary crystallographic data for this article. These data can be obtained free of charge from The Cambridge Crystallographic Data Center via www.ccdc.cam.ac.uk/data_request/cif.

Computational Details

All DFT calculations were done with the TURBOMOLE program package (version 7.8),[53,54] employing the resolution-of-the-identity (RI) approximation. Unless further specified, geometries were optimized in vacuum using RI-DFT (modules ridft and rdgrad)[55–57] with the PBE0[58–60] functional in the def2-SVP basis set[56,61] with the m5 grid[55] and a self-consistent field (SCF) energy convergence threshold of 10^{-8}. All molecular structures together with their DFT energies are available from the "Computational Data.zip" file as part of the Supporting Information. Final properties of complex **1** (i.e., bond indices and spectra) were calculated at a geometry with tighter convergence thresholds, both for the MOs (SCF energy convergence: 10^{-10}) and during the structure optimization (energy convergence: 10^{-9}; Cartesian gradient convergence: 10^{-4}), with grid 5 in the def2-TZVP[56,61] basis set. MBIs[62] were calculated with the proper module. IR absorption spectra were calculated using analytic Hessians for the harmonic frequencies (with the aoforce module).[63] To model the experimental UV/vis absorption spectra of complex **1** in solution, vertical electronic excitation energies (VEEs) and oscillator strengths were calculated using TDDFT (using the escf module)[64,65] with the PBE0 functional and the def2-TZVP basis set. To account for solvation effects on the VEEs, the implicit solvent model COSMO (Conductor-like screening model)[66] with settings for acetonitrile (relative dielectric constant $\varepsilon_r = 37.5$ and refractive index $n = 1.344$) was used.

For the stability analysis of the tetra- versus trinuclear complexes, differences in the Gibbs free energy in solution (G_{tot}) were calculated. Geometries for all species have been optimized at the finer PBE0/def2-TZVP level of theory with tightened convergence criteria (vide supra). The final DFT energy in vacuum was used as the electronic contribution (E_{el}) to G_{tot}. The thermal contributions (E_{th}) have been calculated using the rigid-rotor–harmonic-oscillator model at 25 °C (using freeh) based on the harmonic frequencies calculated at the DFT level.

Gibbs free energies of solvation (δG_{solv}) were calculated with the conductor-like screening model for real solvents (COSMO-RS) at the BP-TZVPD-FINE level of theory as implemented in COSMO*therm* (version 2021).[67] For these calculations, the geometries were reoptimized with the BP86[68,69] functional in the def-TZVP basis set[56,61] in both vacuum and in the so-called conductor-limit (i.e., assuming $\varepsilon = \infty$ for the dielectric constant) of COSMO.[66] Details on COSMO and COSMO-RS, as well as the precise computational protocol for δG_{solv} can be found elsewhere.[70,71] A temperature of 25 °C and a molar fraction of 100% for the solvent (methanol, diethyl ether, tetrahydrofuran, and cyclohexane) and vanishing concentrations ($x = 0$) for the complexes as solutes were used. Finally, the total Gibbs free energy of each species at 25 °C in solution (G_{tot}) was obtained as a sum of the electronic, thermal, and solvation contributions as individually described above.

$$G_{tot} = E_{el} + E_{th} + \delta G_{solv} \quad (4)$$

Acknowledgements

The authors acknowledge support from the University of Duisburg-Essen (S.S.). The authors are thankful to Beate Römer for elemental analyses, Julian Grahl for the UV/vis measurement, and Joana Tewes for the lab work support.

Open Access funding enabled and organized by Projekt DEAL.

Conflict of Interest

The authors declare no conflict of interest.

Author Contributions

Timo Fockenberg: synthesis, characterization, writing manuscript draft. **Niklas Sülzner**: DFT calculations, writing manuscript draft and revision. **Hatem M. A. Amin**: electrochemical measurements, writing manuscript draft and revision. **Christoph Wölper**: sc-XRD measurements. **Christof Hättig**: supervision, manuscript revision. **Stephan Schulz**: conceptualization, supervision, project administration, manuscript revision. The manuscript was written through contributions of all authors. All authors have given approval to the final version of the manuscript.

Data Availability Statement

The data that support the findings of this study are available in the supplementary material of this article.

Keywords: cobalt (III) carboxylates · cyclic voltammetry · DFT calculations · single-crystal X-ray diffraction

[1] F. Cavani, J. H. Teles, *ChemSusChem* **2009**, *2*, 508.
[2] R. Matheu, P. Garrido-Barros, M. Gil-Sepulcre, M. Z. Ertem, X. Sala, C. Gimbert-Suriñach, A. Llobet, *Nat. Rev. Chem.* **2019**, *3*, 331.
[3] J. Song, C. Wei, Z. F. Huang, C. Liu, L. Zeng, X. Wang, Z. J. Xu, *Chem. Soc. Rev.* **2020**, *49*, 2196.
[4] S. Saddeler, U. Hagemann, S. Schulz, *Inorg. Chem.* **2020**, *59*, 10013.
[5] D. Waffel, E. Budiyanto, T. Porske, J. Büker, T. Falk, Q. Fu, S. Schmidt, H. Tüysüz, M. Muhler, B. Peng, *Mol. Catal.* **2020**, *498*, 111251.
[6] T. Falk, E. Budiyanto, M. Dreyer, C. Pflieger, D. Waffel, J. Büker, C. Weidenthaler, K. F. Ortega, M. Behrens, H. Tüysüz, M. Muhler, B. Peng, *ChemCatChem* **2021**, *13*, 2942.
[7] T. Falk, S. Anke, H. Hajiyani, S. Saddeler, S. Schulz, R. Pentcheva, B. Peng, M. Muhler, *Catal. Sci. Technol.* **2021**, *11*, 7552.
[8] J. Amtawong, A. I. Nguyen, T. D. Tilley, *J. Am. Chem. Soc.* **2022**, *144*, 1475.
[9] A. I. Nguyen, M. S. Ziegler, P. Oña-Burgos, M. Sturzbecher-Hohne, W. Kim, D. E. Bellone, T. D. Tilley, *J. Am. Chem. Soc.* **2015**, *137*, 12865.
[10] F. Song, R. Moré, M. Schilling, G. Smolentsev, N. Azzaroli, T. Fox, S. Luber, G. R. Patzke, *J. Am. Chem. Soc.* **2017**, *139*, 14198.
[11] M. D. Symes, Y. Surendranath, D. A. Lutterman, D. G. Nocera, *J. Am. Chem. Soc.* **2011**, *133*, 5174.
[12] P. F. Smith, C. Kaplan, J. E. Sheats, D. M. Robinson, N. S. McCool, N. Mezle, G. C. Dismukes, *Inorg. Chem.* **2014**, *53*, 2113.
[13] X. Li, E. B. Clatworthy, A. F. Masters, T. Maschmeyer, *Chem. Eur. J.* **2015**, *21*, 16578.
[14] J. K. Beattie, T. W. Hambley, J. A. Klepetko, A. F. Masters, P. Turner, *Polyhedron* **1998**, *17*, 1343.
[15] R. Chakrabarty, B. K. Das, *J. Mol. Catal. A: Chem.* **2004**, *223*, 39.
[16] B. K. Das, J. H. Clark, *Chem. Commun.* **2000**, *7*, 605.
[17] R. Chakrabarty, S. J. Bora, B. K. Das, *Inorg. Chem.* **2007**, *46*, 9450.
[18] R. Chakrabarty, D. Kalita, B. K. Das, *Polyhedron* **2007**, *26*, 1239.
[19] B. K. Das, R. Chakrabarty, *J. Chem. Sci.* **2011**, *123*, 163.
[20] R. Chakrabarty, P. Sarmah, B. Saha, S. Chakravorty, B. K. Das, *Inorg. Chem.* **2009**, *48*, 6371.
[21] P. Sarmah, R. Chakrabarty, P. Phukan, B. K. Das, *J. Mol. Catal. A: Chem.* **2007**, *268*, 36.
[22] R. Chakrabarty, B. K. Das, J. H. Clark, *Green Chem.* **2007**, *9*, 845.
[23] P. Sarmah, B. K. Das, *Indian J. Chem., Sect. A.* **2014**, *53*, 41.
[24] J. G. McAlpin, T. A. Stich, C. A. Ohlin, Y. Surendranath, D. G. Nocera, W. H. Casey, R. D. Britt, *J. Am. Chem. Soc.* **2011**, *133*, 15444.
[25] R. G. Hadt, D. Hayes, C. N. Brodsky, A. M. Ullman, D. M. Casa, M. H. Upton, D. G. Nocera, L. X. Chen, *J. Am. Chem. Soc.* **2016**, *138*, 11017.
[26] C. N. Brodsky, R. G. Hadt, D. Hayes, B. J. Reinhart, N. Li, L. X. Chen, D. G. Nocera, *PNAS* **2017**, *114*, 3855.
[27] J. Amtawong, B. B. Skjelstad, D. Balcells, T. D. Tilley, *Inorg. Chem.* **2020**, *59*, 15553.
[28] A. I. Nguyen, J. Wang, D. S. Levine, M. S. Ziegler, T. D. Tilley, *Chem. Sci.* **2017**, *8*, 4274.
[29] M. W. Ishaq, R. Nawaz, A. Jalil, M. A. Hashmi, T. Zheng, L. Li, *J. Mol. Struct.* **2021**, *1235*, 130216.
[30] S. Berardi, G. La Ganga, M. Natali, I. Bazzan, F. Puntoriero, A. Sartorel, F. Scandola, S. Campagna, M. Bonchio, *J. Am. Chem. Soc.* **2012**, *134*, 11104.
[31] Y. Wang, F. Li, X. Zhou, F. Yu, J. Du, L. Bai, L. Sun, *Angew. Chem. Int. Ed.* **2017**, *56*, 6911; Angew. Chem. 2017, 129, 7015.
[32] Z. Luo, Y. Hou, J. Zhang, S. Wang, X. Wang, *Beilstein J. Org. Chem.* **2018**, *14*, 2331.
[33] S. Gutiérrez-Tarriño, J. Gaona-Miguélez, P. Oña-Burgos, *Dalton Trans.* **2021**, *50*, 15370.
[34] F. Evangelisti, R. Güttinger, R. Moré, S. Luber, G. R. Patzke, *J. Am. Chem. Soc.* **2013**, *135*, 18734.
[35] A. Scheurer, J. Korzekwa, T. Nakajima, F. Hampel, A. Buling, C. Derks, M. Neumann, L. Joly, K. Petukhov, K. Gieb, P. Müller, K. Kuepper, K. Meyer, *Eur. J. Inorg. Chem.* **2015**, *2015*, 1892.
[36] S. J. Bharali, B. K. Das, *Z. Anorg. Allg. Chem.* **2021**, *647*, 794.
[37] J. K. Beattie, J. A. Klepetko, A. F. Masters, P. Turner, *Polyhedron* **2003**, *22*, 947.
[38] C. E. J. Sumner, *Inorg. Chem.* **1988**, *27*, 1320.
[39] Q. Zeng, F. W. Lewis, L. M. Harwood, F. Hartl, *Coord. Chem. Rev.* **2015**, *304–305*, 88.
[40] D. W. Crandell, S. Xu, J. M. Smith, M. H. Baik, *Inorg. Chem.* **2017**, *56*, 4435.
[41] C. J. Richmond, S. Escayola, A. Poater, *Eur. J. Inorg. Chem.* **2019**, *2019*, 2101.
[42] S. A. Chavan, D. Srinivas, P. Ratnasamy, *J. Catal.* **2001**, *204*, 409.
[43] H. J. Eppley, H.-L. Tsai, N. De Vries, K. Felting, G. Christou, D. N. Hendrickson, *J. Am. Chem. Soc.* **1995**, *117*, 301.
[44] T. G. Mayerhöfer, S. Pahlow, J. Popp, *ChemPhysChem.* **2020**, *21*, 2029.
[45] T. C. Davenport, H. S. Ahn, M. S. Ziegler, T. D. Tilley, *Chem. Commun.* **2014**, *50*, 6326.
[46] S. Li, Z. Zhang, W. R. Marks, X. Huang, H. Chen, D. C. Stoian, R. Erni, C. A. Triana, G. R. Patzke, *Nat. Commun.* **2024**, *15*, 8432.
[47] M. Masahiro, N. Yuko, I. Ayumi, O. Mika, Y. Daisuke, S. Hiroshi, H. Makoto, T. Motohiro, *Molecules* **2022**, *27*, 4211.
[48] M. Mikuriya, Y. Naka, D. Yoshioka, M. Handa, *X-Ray Struct. Anal. Online* **2016**, *32*, 55.
[49] G. M. Sheldrick, *Acta Crystallogr.* **1990**, *A46*, 467.
[50] G. M. Sheldrick, *Acta Crystallogr., Sect. C: Struct. Chem.* **2015**, *71*, 3.
[51] C. B. Hübschle, G. M. Sheldrick, B. Dittrich, *J. Appl. Cryst.* **2011**, *44*, 1281.
[52] P. Van Der Sluis, A. L. Spek, *Acta Crystallogr.* **1990**, *A46*, 194.
[53] TURBOMOLE V7.8 2023, a development of University of Karlsruhe and Forschungszentrum Karlsruhe GmbH, 1989-2007, TURBOMOLE GmbH, since 2007; available from https://www.turbomole.org.
[54] Y. J. Franzke, C. Holzer, J. H. Andersen, T. Begušić, F. Bruder, S. Coriani, F. Della Sala, E. Fabiano, D. A. Fedotov, S. Fürst, S. Gillhuber, R. Grotjahn, M. Kaupp, M. Kehry, M. Krstić, F. Mack, S. Majumdar, B. D. Nguyen, S. M. Parker, F. Pauly, A. Pausch, E. Perlt, G. S. Phun, A. Rajabi, D. Rappoport, B. Samal, T. Schrader, M. Sharma, E. Tapavicza, R. S. Treß, V. Voora, A. Wodyński, J. M. Yu, B. Zerulla, F. Furche, C. Hättig, M. Sierka, D. P. Tew, F. Weigend, *J. Chem. Theory Comput.* **2023**, *19*, 6859.
[55] K. Eichkorn, F. Weigend, O. Treutler, R. Ahlrichs, *Theor. Chem. Acc.* **1997**, *97*, 119.
[56] K. Eichkorn, O. Treutler, H. Öhm, M. Häser, R. Ahlrichs, *Chem. Phys. Lett.* **1995**, *242*, 652.
[57] O. Treutler, R. Ahlrichs, *J. Chem. Phys.* **1995**, *102*, 346.
[58] J. P. Perdew, Y. Wang, *Phys. Rev. Lett.* **1994**, *45*, 13244.
[59] J. P. Perdew, K. Burke, M. Ernzerhof, *Phys. Rev. Lett.* **1996**, *77*, 3865.
[60] J. P. Perdew, M. Ernzerhof, K. Burke, *J. Chem. Phys.* **1996**, *105*, 9982.
[61] F. Weigend, R. Ahlrichs, *Phys. Chem. Chem. Phys.* **2005**, *7*, 3297.
[62] I. Mayer, *J. Comput. Chem.* **2007**, *28*, 204.
[63] P. Deglmann, K. May, F. Furche, R. Ahlrichs, *Chem. Phys. Lett.* **2004**, *384*, 103.
[64] R. Bauernschmitt, R. Ahlrichs, *Chem. Phys. Lett.* **1996**, *256*, 454.
[65] R. Bauernschmitt, M. Häser, O. Treutler, R. Ahlrichs, *Chem. Phys. Lett.* **1997**, *264*, 573.
[66] A. Schäfer, A. Klamt, D. Sattel, J. C. W. Lohrenz, F. Eckert, *Phys. Chem. Chem. Phys.* **2000**, *2*, 2187.
[67] BIOVIA COSMOtherm, Release, Dassault Systèmes, https://www.3ds.com.
[68] A. D. Becke, *Phys. Rev. A* **1988**, *38*, 3098.
[69] J. P. Perdew, *Phys. Rev. B* **1986**, *33*, 8822.
[70] A. Hellweg, F. Eckert, *AIChE J.* **2017**, *63*, 3944.
[71] A. Klamt, *WIREs Comput. Mol. Sci.* **2018**, *8*, 1.

Manuscript received: April 2, 2025
Revised manuscript received: June 4, 2025
Version of record online: